JOURNAL OF GUIDANCE, CONTROL, AND DYNAMICS
Vol. 28, No. 1, January–February 2005

Real-Time Attitude-Independent Three-Axis Magnetometer Calibration

John L. Crassidis* and Kok-Lam Lai†
University at Buffalo, State University of New York, Amherst, New York 14260-4400
and
Richard R. Harman‡
NASA Goddard Space Flight Center, Greenbelt, Maryland 20771

New real-time approaches for three-axis magnetometer sensor calibration are derived. These approaches rely on a conversion of the magnetometer-body and geomagnetic-reference vectors into an attitude-independent observation by using scalar checking. The goal of the full calibration problem involves the determination of the magnetometer bias vector, scale factors, and nonorthogonality corrections. Although the actual solution to this full calibration problem involves the minimization of a quartic loss function, the problem can be converted into a quadratic loss function by a centering approximation. This leads to a simple batch linear least-squares solution, which is easily converted into a sequential algorithm that can be executed in real time. Alternative real-time algorithms are also developed based on both the extended Kalman filter and Unscented filter. With these real-time algorithms, a full magnetometer calibration can now be performed on-orbit during typical spacecraft mission-mode operations. The algorithms are tested using both simulated data of an Earth-pointing spacecraft and actual data from the Transition Region and Coronal Explorer.

Introduction

THREE-AXIS magnetometers (TAMs) are widely used for onboard spacecraft operations. The basic concept behind these devices is a fairly simple one, involving a simple magnetic sensor coupled with an electronics unit to provide data in a digital format. These sensors are useful because they provide both the direction and magnitude of the magnetic field, and they are lightweight, reliable, and have low-power requirements, with no moving parts.[1] For these reasons, most low-Earth orbiting spacecraft (below 1000 km) have TAMs as part of their basic sensor package. It is well known that a TAM can be used to determine a three-axis attitude when coupled with gyros or a dynamic model in an extended Kalman filter (see Ref. 2). Attitude-knowledge accuracies of 1–2 deg are common using this approach, which can be improved by using well-calibrated sensors to achieve accuracies of 0.1–0.5 deg (Ref. 3). An exciting new area of research involves using a TAM together with rate and sun sensor measurements for orbit (position) estimation. Accuracies on the order of 10–100 km can be achieved, which is within the position-knowledge requirements of many spacecraft.[4,5] These studies clearly show that an integrated magnetometer-based attitude/orbit estimation system can provide the necessary knowledge requirements of a spacecraft in a single package.

A paramount issue to the attitude accuracy obtained using magnetometer measurements is the precision of the onboard calibration. The accuracy obtained using a TAM depends on a number of factors, including biases, scale factors, and nonorthogonality corrections. Scale factors and nonorthogonality corrections occur because the individual magnetometer axes are not orthonormal, typically due to thermal gradients within the magnetometer or to mechanical stress from the spacecraft.[6] Magnetometer calibration is often accomplished using batch methods, where an entire set of data must be stored to determine the unknown parameters. This process is often repeated many times during the lifetime of a spacecraft to ensure the best possible precision obtained from magnetometer measurements.

If an attitude is known accurately, then the magnetometer calibration problem is easy to solve. However, this is generally not the case. Fortunately, an attitude-independent scalar observation can be obtained using the norms of the body-measurement and geomagnetic-reference vectors. For the noise-free case, these norms are identical because the attitude matrix preserves the length of a vector. This process is also known as scalar checking.[7] Unfortunately, even for the simpler magnetometer-bias determination problem, the loss function to be minimized is quartic in nature. The most common technique to overcome this difficulty has been proposed by Gambhir, who applies a "centering" approximation to yield a quadratic loss function that can be minimized using simple linear least squares.[8] Alonso and Shuster[9] expand on Gambhir's approach by using a second step that employs the centered estimate as an initial value to an iterative Gauss–Newton method. Their algorithm, called TWOSTEP,[9] has been shown to perform well when other algorithms fail due to divergence problems. Furthermore, Alonso and Shuster have extended this approach to perform a complete calibration involving biases as well as scale factors and nonorthogonality corrections.[6]

One of the current goals for modern-day spacecraft is the ability to perform onboard and autonomous calibrations in real time without ground support. The TWOSTEP algorithm requires an iterative process on a batch of data, and so it cannot be performed in real time. The main objective of this paper is to present and compare several sequential algorithms that are suitable for real-time applications. The centering approximation leads to a non-iterative least-squares solution and has been shown to be nearly optimal for many realistic cases.[10] Because this approximation is linear, it can be converted into a sequential process, which is the first real-time algorithm shown in this paper. The second algorithm uses an extended Kalman filter approach that is developed with commonly employed estimation techniques. The third algorithm uses an Unscented filter approach that offers very good results for robust calibration when the initial conditions are poorly known. Simulated test cases and results using real data obtained from the Transition Region and Coronal

Received 5 November 2003; revision received 23 April 2004; accepted for publication 24 April 2004.

*Associate Professor, Department of Mechanical and Aerospace Engineering; johnc@eng.buffalo.edu. Associate Fellow AIAA.
†Graduate Student, Department of Mechanical and Aerospace Engineering; klai2@eng.buffalo.edu. Student Member AIAA.
‡Aerospace Engineer, Flight Dynamics Analysis Branch; richard.r.harman@nasa.gov.

Explorer (TRACE) spacecraft show the validity of the new real-time algorithms to perform onboard and autonomous calibrations.

Measurement Model

In this section, the TAM measurement model and attitude-independent observation are summarized. More details on these concepts may be found in Ref. 6. The magnetometer measurements can be modeled as

$$\boldsymbol{B}_k = (I_{3\times 3} + D)^{-1}\left(\mathcal{O}^T A_k \boldsymbol{H}_k + \boldsymbol{b} + \boldsymbol{\epsilon}_k\right), \qquad k = 1,\ 2,\ \ldots,\ N \tag{1}$$

where $\boldsymbol{B}_k$ is the measurement of the magnetic field by the magnetometer at time t_k, $\boldsymbol{H}_k$ is the corresponding value of the geomagnetic field with respect to an Earth-fixed coordinate system, A_k is the unknown attitude matrix of the magnetometer with respect to the Earth-fixed coordinates, D is an unknown fully populated matrix of scale factors (the diagonal elements) and non-orthogonality corrections (the off-diagonal elements), $\mathcal{O}$ is an orthogonal matrix, $\boldsymbol{b}$ is the bias vector, and $\boldsymbol{\epsilon}_k$ is the measurement noise vector that is assumed to be a zero-mean Gaussian process with covariance Σ_k. (See Ref. 6 for a discussion on the physical connotations of the $\mathcal{O}$ matrix.) The matrix D can be assumed to be symmetric without loss of generality. Also, $I_{n\times n}$ is an $n \times n$ identity matrix. The goal of the full calibration problem is to estimate D and $\boldsymbol{b}$. We first define the following quantities:

$$\boldsymbol{\theta} \equiv [\boldsymbol{b}^T \quad \boldsymbol{D}^T]^T \tag{2a}$$

$$\boldsymbol{D} \equiv [D_{11} \quad D_{22} \quad D_{33} \quad D_{12} \quad D_{13} \quad D_{23}]^T \tag{2b}$$

$$E \equiv 2D + D^2 \tag{2c}$$

$$\boldsymbol{c} \equiv (I_{3\times 3} + D)\boldsymbol{b} \tag{2d}$$

$$S_k \equiv \begin{bmatrix} B_{1_k}^2 & B_{2_k}^2 & B_{3_k}^2 & 2B_{1_k}B_{2_k} & 2B_{1_k}B_{3_k} & 2B_{2_k}B_{3_k} \end{bmatrix} \tag{2e}$$

$$\boldsymbol{E} \equiv [E_{11} \quad E_{22} \quad E_{33} \quad E_{12} \quad E_{13} \quad E_{23}]^T \tag{2f}$$

An attitude-independent observation can be computed from

$$z_k \equiv \|\boldsymbol{B}_k\|^2 - \|\boldsymbol{H}_k\|^2 = L_k\boldsymbol{\theta}' - \|\boldsymbol{b}(\boldsymbol{\theta}')\|^2 + v_k \tag{3}$$

where

$$L_k \equiv \begin{bmatrix} 2\boldsymbol{B}_k^T & -S_k \end{bmatrix} \tag{4a}$$

$$\boldsymbol{\theta}' \equiv [\boldsymbol{c}^T \quad \boldsymbol{E}^T]^T \tag{4b}$$

$$v_k \equiv 2[(I_{3\times 3} + D)\boldsymbol{B}_k - \boldsymbol{b}]^T\boldsymbol{\epsilon}_k - \|\boldsymbol{\epsilon}_k\|^2 \tag{4c}$$

The effective measurement noise v_k is approximately Gaussian with mean denoted by μ_k and variance denoted by σ_k^2, each given by

$$\mu_k \equiv E\{v_k\} = -\mathrm{tr}(\Sigma_k) \tag{5a}$$

$$\sigma_k^2 \equiv E\left\{v_k^2\right\} - \mu_k^2 = 4[(I_{3\times 3} + D)\boldsymbol{B}_k - \boldsymbol{b}]^T\Sigma_k[(I_{3\times 3} + D)\boldsymbol{B}_k - \boldsymbol{b}] + 2\left(\mathrm{tr}\Sigma_k^2\right) \tag{5b}$$

$$\Sigma_k = E\left\{\boldsymbol{\epsilon}_k\boldsymbol{\epsilon}_k^T\right\} \tag{5c}$$

where $E\{\,\}$ denotes expectation. Note that the measurement variance in Eq. (5b) is a function of the unknown parameters. A conversion from $\boldsymbol{c}$ and E to the sought variables $\boldsymbol{b}$ and D may be found in Ref. 6.

Sequential Centered Algorithm

The measurement model in Eq. (3) is clearly nonlinear in the unknown parameter vector $\boldsymbol{\theta}'$. Therefore, linear least squares cannot be applied directly. However, it is possible to determine an approximate linear solution by applying a centering approach. The complete batch algorithm is shown in Ref. 6. Because this solution is linear, then a sequential formulation can be derived that provides real-time estimates. A formal derivation of this process may be found in Ref. 11; we present only the final algorithm here. First, the sequential formulas for the averaged quantities are given by

$$\bar{L}_{k+1} = \left[1\Big/\left(\sigma_{k+1}^2 + \bar{\sigma}_k^2\right)\right]\left(\sigma_{k+1}^2\bar{L}_k + \bar{\sigma}_k^2 L_{k+1}\right) \tag{6a}$$

$$\bar{z}_{k+1} = \left[1\Big/\left(\sigma_{k+1}^2 + \bar{\sigma}_k^2\right)\right]\left(\sigma_{k+1}^2\bar{z}_k + \bar{\sigma}_k^2 z_{k+1}\right) \tag{6b}$$

$$\bar{\mu}_{k+1} = \left[1\Big/\left(\sigma_{k+1}^2 + \bar{\sigma}_k^2\right)\right]\left(\sigma_{k+1}^2\bar{\mu}_k + \bar{\sigma}_k^2 \mu_{k+1}\right) \tag{6c}$$

where

$$1\Big/\bar{\sigma}_{k+1}^2 = 1\Big/\bar{\sigma}_k^2 + 1\Big/\sigma_{k+1}^2 \tag{7}$$

Next, the following centered variables are defined:

$$\tilde{L}_{k+1} \equiv L_{k+1} - \bar{L}_{k+1} \tag{8a}$$

$$\tilde{z}_{k+1} \equiv z_{k+1} - \bar{z}_{k+1} \tag{8b}$$

$$\tilde{\mu}_{k+1} \equiv \mu_{k+1} - \bar{\mu}_{k+1} \tag{8c}$$

Finally, the sequential formulas for the optimal centered estimate of $\boldsymbol{\theta}'$, denoted by $\tilde{\boldsymbol{\theta}}'^*$, and covariance of $\tilde{\boldsymbol{\theta}}'^*$, denoted by $\tilde{P}_{\theta'\theta'}$, are given by

$$\tilde{\boldsymbol{\theta}}'^*_{k+1} = K_k\tilde{\boldsymbol{\theta}}'^*_k + \left(1\Big/\sigma_{k+1}^2\right)(\tilde{z}_{k+1} - \tilde{\mu}_{k+1})\,\tilde{P}_{\theta'\theta'_{k+1}}\tilde{L}_{k+1}^T \tag{9a}$$

$$\tilde{P}_{\theta'\theta'_{k+1}} = K_k\tilde{P}_{\theta'\theta'_k} \tag{9b}$$

$$K_k \equiv I_{9\times 9} - \tilde{P}_{\theta'\theta'_k}\tilde{L}_{k+1}^T\left(\tilde{L}_{k+1}\tilde{P}_{\theta'\theta'_k}\tilde{L}_{k+1}^T + \sigma_{k+1}^2\right)^{-1}\tilde{L}_{k+1} \tag{9c}$$

Note that only an inverse of a scalar quantity is required in the sequential process. The sequential process can be initialized using a small batch of data. A conversion from $\tilde{P}_{\theta'\theta'}$ to the covariance of the parameters $\boldsymbol{b}$ and $\boldsymbol{D}$ may be found in Ref. 6. Also, an approach for determining σ_{k+1}^2 involves using the earlier estimate in Eq. (5b).

Kalman Filter Formulation

In this section, an extended Kalman filter (EKF) is derived to determine the calibration parameters in real time. An advantage of the EKF formulation over the sequential centered approach is that $\boldsymbol{b}$ and $\boldsymbol{D}$ can be computed directly without a conversion from $\boldsymbol{c}$ and $\boldsymbol{E}$. A summary of the EKF equations may be found in Ref. 12. Because the vector $\boldsymbol{\theta}$ in Eq. (2a) is constant, then the state model is given by $\dot{\hat{\boldsymbol{x}}}(t) = \boldsymbol{0}$, where $\hat{\boldsymbol{x}} \equiv \boldsymbol{\theta}^*$, which is used to denote the optimal estimate of $\boldsymbol{\theta}$. The measurement model is given by $z_k = h_k(\boldsymbol{x}_k) + v_k$, where

$$h_k(\boldsymbol{x}_k) \equiv -\boldsymbol{B}_k^T\left(2D_k + D_k^2\right)\boldsymbol{B}_k + 2\boldsymbol{B}_k^T(I_{3\times 3} + D_k)\boldsymbol{b}_k - \|\boldsymbol{b}_k\|^2 \tag{10}$$

Because no process noise appears in the state model, then the updated quantities (state and covariance) are given by their respective propagated quantities. The EKF equations then reduce down to

$$\hat{\boldsymbol{x}}_{k+1} = \hat{\boldsymbol{x}}_k + K_k[z_{k+1} - h_{k+1}(\hat{\boldsymbol{x}}_k)] \tag{11a}$$

$$P_{k+1} = [I_{9\times 9} - K_k H_{k+1}(\hat{\boldsymbol{x}}_k)]P_k \tag{11b}$$

$$K_k = P_k H_{k+1}^T(\hat{\boldsymbol{x}}_k)\left[H_{k+1}(\hat{\boldsymbol{x}}_k)P_k H_{k+1}^T(\hat{\boldsymbol{x}}_k) + \sigma_{k+1}^2(\hat{\boldsymbol{x}}_k)\right]^{-1} \tag{11c}$$

where $P \equiv P_{\theta\theta}$, which is the covariance of the estimated parameters for $\boldsymbol{b}$ and $\boldsymbol{D}$. The state dependence of the measurement variance is shown through Eq. (5b). The 1×9 matrix $H(\boldsymbol{x})$ is the partial derivative of $h(\boldsymbol{x})$ with respect to $\boldsymbol{x}$. This quantity is given by

$$H(\boldsymbol{x}) = \left[2\boldsymbol{B}^T(I_{3\times 3} + D) - 2\boldsymbol{b}^T \quad -S\frac{\partial \boldsymbol{E}}{\partial \boldsymbol{D}} + 2J\right] \tag{12}$$

where S is defined in Eq. (2e) and

$$\frac{\partial \boldsymbol{E}}{\partial \boldsymbol{D}} = \begin{bmatrix} 2(1+D_{11}) & 0 & 0 & 2D_{12} & 2D_{13} & 0 \\ 0 & 2(1+D_{22}) & 0 & 2D_{12} & 0 & 2D_{23} \\ 0 & 0 & 2(1+D_{33}) & 0 & 2D_{13} & 2D_{23} \\ D_{12} & D_{12} & 0 & 2+D_{11}+D_{22} & D_{23} & D_{13} \\ D_{13} & 0 & D_{13} & D_{23} & 2+D_{11}+D_{33} & D_{12} \\ 0 & D_{23} & D_{23} & D_{13} & D_{12} & 2+D_{22}+D_{33} \end{bmatrix} \tag{13a}$$

$$J \equiv [B_1 b_1 \quad B_2 b_2 \quad B_3 b_3 \quad B_1 b_2 + B_2 b_1 \quad B_1 b_3 + B_3 b_1 \quad B_2 b_3 + B_3 b_2] \tag{13b}$$

The sensitivity matrix $H(\hat{\boldsymbol{x}})$ in the EKF evaluates $H(\boldsymbol{x})$ at its current estimate, and the notations $h_{k+1}(\hat{\boldsymbol{x}}_k)$, $H_{k+1}(\hat{\boldsymbol{x}}_k)$ and $\sigma^2_{k+1}(\hat{\boldsymbol{x}}_k)$ denote an evaluation at the $k+1$ time-step measurement using $\boldsymbol{B}_{k+1}$ and at the k time-step estimate using $\hat{\boldsymbol{x}}_k$.

Unscented Filter Formulation

In this section, a new approach, developed by Julier et al.[13] is discussed as an alternative to the EKF. This approach, which they called the Unscented filter (UF), works on the premise that with a fixed number of parameters it should be easier to approximate a Gaussian distribution than to approximate an arbitrary nonlinear function. The UF uses a different propagation than the form given by the standard EKF. Given an $n \times n$ covariance matrix P, a set of order n points can be generated from the columns (or rows) of the matrices $\pm\sqrt{(nP)}$. The set of points is zero mean, but if the distribution has mean $\boldsymbol{\mu}$, then simply adding $\boldsymbol{\mu}$ to each of the points yields a symmetric set of $2n$ points having the desired mean and covariance. Because to the symmetric nature of this set, its odd central moments are zero, and so its first three moments are the same as the original Gaussian distribution. (See Ref. 14 for more details.)

The implementation of the UF for real-time magnetometer calibration is straightforward. First, the following set of sigma points are computed from $P \equiv P_{\theta\theta}$:

$$\boldsymbol{\sigma}_k \leftarrow 2n \text{ columns from } \pm\gamma\sqrt{P_k} \tag{14a}$$

$$\boldsymbol{\chi}_k(0) = \hat{\boldsymbol{x}}_k \tag{14b}$$

$$\boldsymbol{\chi}_k(i) = \boldsymbol{\sigma}_k(i) + \hat{\boldsymbol{x}}_k, \qquad i = 1, 2, \ldots, 2n \tag{14c}$$

The parameter γ is given by $\gamma = \sqrt{(n+\lambda)}$, where the composite scaling parameter λ is given by $\lambda = \alpha^2(n+\kappa) - n$. The constant α determines the spread of the sigma points and is usually set to a small positive value, for example, $1 \times 10^{-4} \leq \alpha \leq 1$ (Ref. 14). Also, the parameter κ is usually given by $\kappa = 3 - n$. Efficient methods to compute the matrix square root can be found by using the Cholesky decomposition (see Ref. 15). The following weights are now defined:

$$W_0^{\text{mean}} = \lambda/(n+\lambda) \tag{15a}$$

$$W_0^{\text{cov}} = \lambda/(n+\lambda) + (1 - \alpha^2 + \beta) \tag{15b}$$

$$W_i^{\text{mean}} = W_i^{\text{cov}} = 1/2(n+\lambda), \qquad i = 1, 2, \ldots, 2n \tag{15c}$$

where β is used to incorporate prior knowledge of the distribution.

Because the state model estimate is given by $\hat{\boldsymbol{x}}(t) = \boldsymbol{0}$, then the propagated values for the state and covariance are given by their respective updated values, which significantly reduces the computational requirements in the UF. Hence, the only essential difference between the EKF and UF formulations is in the computation of the innovations covariance, where the EKF uses a first-order expansion to compute this quantity, whereas the UF uses a nonlinear transformation to compute this quantity. For the TAM calibration algorithm using the UF, the state estimate is calculated by

$$\hat{\boldsymbol{x}}_{k+1} = \hat{\boldsymbol{x}}_k + K_k(z_{k+1} - \hat{z}_k) \tag{16}$$

where $\hat{z}_k$ is the mean observation, given by

$$\hat{z}_k = \sum_{i=0}^{2n} W_i^{\text{mean}} h_{k+1}[\boldsymbol{\chi}_k(i)] \tag{17}$$

where $h_{k+1}[\boldsymbol{\chi}_k(i)]$ is defined in Eq. (10). Note that $h_{k+1}[\boldsymbol{\chi}_k(i)]$ denotes an evaluation at the $k+1$ time-step measurement using $\boldsymbol{B}_{k+1}$ and at the k time-step sigma point using $\boldsymbol{\chi}_k(i)$. The gain K_k is computed by

$$K_k = P_k^{xz}\left[P_k^{zz} + \sigma^2_{k+1}(\hat{\boldsymbol{x}}_k)\right]^{-1} \tag{18}$$

where P_k^{xz} is the cross-correlation matrix between $\hat{\boldsymbol{x}}_k$ and $\hat{z}_k$ given by

$$P_k^{xz} = \sum_{i=0}^{2n} W_i^{\text{cov}} \left\{\boldsymbol{\chi}_k^x(i) - \hat{\boldsymbol{x}}_k\right\}\{h_{k+1}[\boldsymbol{\chi}_k(i)] - \hat{z}_k\}^T \tag{19}$$

and P_k^{zz} is the output covariance given by

$$P_k^{zz} = \sum_{i=0}^{2n} W_i^{\text{cov}} \{h_{k+1}[\boldsymbol{\chi}_k(i)] - \hat{z}_k\}\{h_{k+1}[\boldsymbol{\chi}_k(i)] - \hat{z}_k\}^T \tag{20}$$

Finally, the propagated covariance is given by

$$P_{k+1} = P_k - K_k\left[P_k^{zz} + \sigma^2_{k+1}(\hat{\boldsymbol{x}}_k)\right]K_k^T \tag{21}$$

New sigma points can now be calculated using P_{k+1} for the sequential UF process.

Another approach for the UF uses the measurement noise model of Eq. (3) with an augmented vector given by the state and $\boldsymbol{\epsilon}$ in Eq. (4c). Therefore, a decomposition of a 12×12 matrix is now required. In the strictest sense, this approach is more optimal than the first approach because the effect of the nonlinear-appearing measurement noise is directly used in the UF. However, the computational requirements are vastly increased due to the decomposition of a higher dimensional augmented matrix. Also, from numerous simulation trials, no apparent advantages to using the augmented approach in the UF is seen. More details on this UF formulation for magnetometer calibration may be found in Ref. 16.

Simulated and Real Data Results

In this section, results of the TWOSTEP, sequential centered, EKF, and UF formulations are shown using both simulated and real data. The simulated spacecraft is modeled after the Tropical Rainfall Measurement Mission spacecraft. This is an Earth-pointing spacecraft (rotating about its y axis) in low Earth orbit (currently near circular at 402 km), with an inclination of 35 deg (Ref. 17). The geomagnetic field is simulated using a 10th-order International Geomagnetic Reference Field model.[18] The magnetometer-body and geomagnetic-reference vectors for the simulated runs each have a magnitude of about 500 mG. The measurement noise is assumed to be white and Gaussian, and the covariance is taken to be isotropic with a standard deviation of 0.5 mG. The measurements are sampled every 10 s over an 8-h span. The true values for the bias $\boldsymbol{b}$ and elements of the D matrix are shown in Table 1. Large values for

Table 1 Results using simulated magnetic field data with white noise

Parameter	Truth	TWOSTEP	Centered	EKF	UF
b_1	50 mG	49.9828 ± 0.4445	49.9720 ± 0.4717	49.3909 ± 5.4206	49.9044 ± 0.4784
b_2	30 mG	29.8409 ± 0.5253	30.1566 ± 6.5670	32.8364 ± 9.7200	29.7297 ± 0.5723
b_3	60 mG	59.9721 ± 0.4642	59.9552 ± 0.6270	55.8104 ± 10.2291	59.9166 ± 0.4987
D_{11}	0.05	0.0500 ± 0.0002	0.0500 ± 0.0002	0.0490 ± 0.0011	0.0499 ± 0.0003
D_{22}	0.10	0.0994 ± 0.0020	0.1001 ± 0.0149	0.1184 ± 0.0478	0.0991 ± 0.0022
D_{33}	0.05	0.0500 ± 0.0003	0.0500 ± 0.0003	0.0490 ± 0.0013	0.0499 ± 0.0003
D_{12}	0.05	0.0499 ± 0.0010	0.0499 ± 0.0010	0.0489 ± 0.0128	0.0498 ± 0.0011
D_{13}	0.05	0.0499 ± 0.0002	0.0499 ± 0.0002	0.0499 ± 0.0006	0.0500 ± 0.0002
D_{23}	0.05	0.0499 ± 0.0010	0.0499 ± 0.0012	0.0410 ± 0.0224	0.0498 ± 0.0012

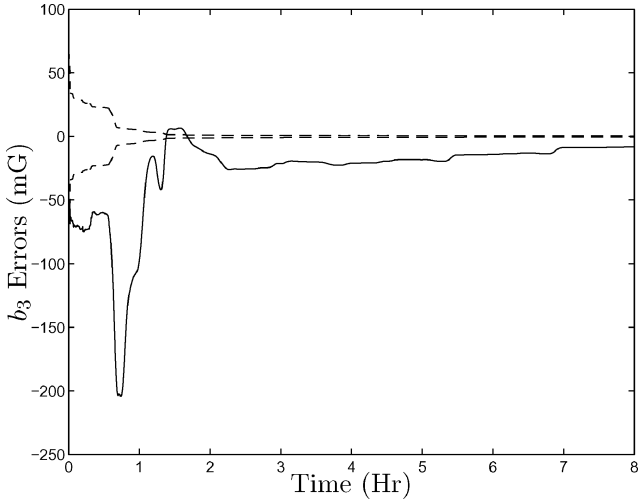

Fig. 1 EKF errors and 3σ bounds for b_3 with white noise.

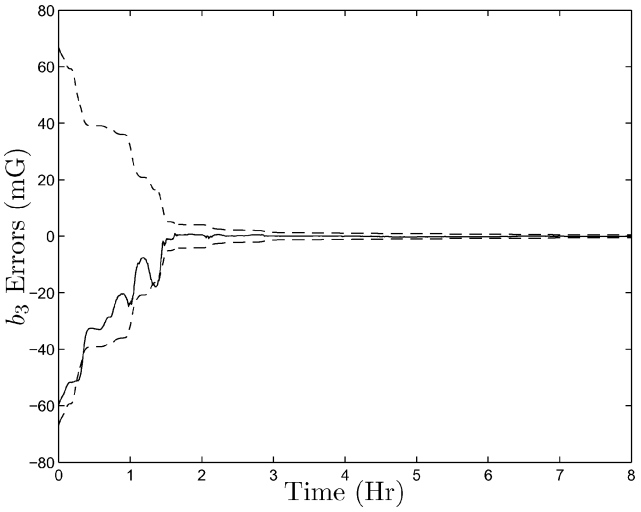

Fig. 2 UF errors and 3σ bounds for b_3 with white noise.

the biases are used to test the robustness of the sequential centered, EKF, and UF algorithms.

There were 1000 runs executed, which provide a Monte Carlo–type simulation. Shown in Table 1 are the averaged batch solutions given by the TWOSTEP and centered algorithms, each with their computed 3σ bounds. All comparisons are made with respect to TWOSTEP. The centered algorithm does a fairly good job at estimating all parameters, with the exception of b_2. This parameter corresponds to the least observable variable, which results in a wide variation from the averaged value.

The EKF and UF are both executed at time $t = 0$ using initial conditions of zeros for all states. The initial covariance matrix is diagonal, given by

$$P_0 = \begin{bmatrix} 500 I_{3\times 3} & 0_{3\times 6} \\ 0_{6\times 3} & 0.001 I_{6\times 6} \end{bmatrix} \tag{22}$$

This assumes a 3σ bound on the initial bias estimates to be about 70 mG and a 3σ bound on the initial estimates for the elements of the D matrix to be about 0.1. The parameters used in the UF are $\alpha = 0.1$, $\beta = 300$, $\kappa = 3 - n$, and $n = 9$. The EKF and UF solutions at the final time are shown in Table 1. The EKF does not converge to the correct solution for many of the parameters, whereas the UF gave results that are just as good as the TWOSTEP solutions. Also, the 3σ bounds for the UF are much smaller than for the EKF and centered algorithm. Even though the mean values of the centered algorithm are slightly better than the UF results, it is important to note the $\pm$ values are more important because they represent the variability over the 1000 Monte-Carlo runs.

Figures 1 and 2 show the EKF and UF errors and 3σ bounds for the parameter b_3 for a typical case. The EKF does not converge to the correct solution during the 8-h simulated run. For this problem, the first-order approximation in the EKF does not adequately capture the large initial errors. The biggest concern with the EKF solutions is the confidence of the results dictated by the 3σ bounds, with b_3

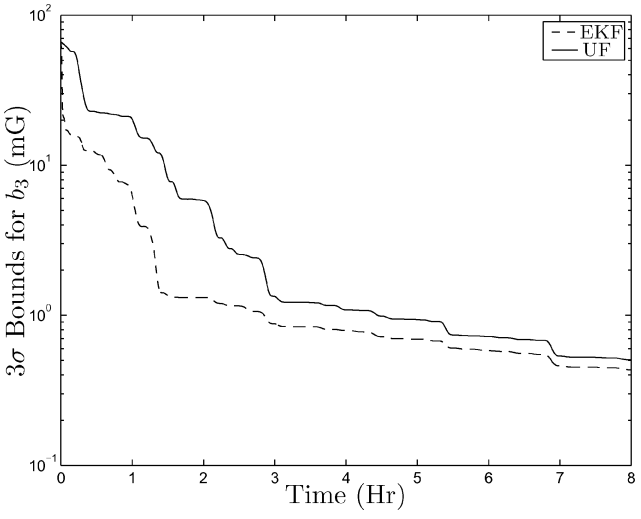

Fig. 3 EKF and UF 3σ bounds for b_3 with white noise.

shown in Fig. 3. In fact, if the truth is not known a priori and we only had the covariance to assess filter performance, Fig. 3 would indicate that the EKF is performing better than the UF. This can certainly provide some misleading results. However, unlike the EKF, the 3σ bounds computed from the 1000 runs associated with the UF are nearly identical to the 3σ bounds computed from the UF covariance for all of the parameters. (The final value shown in Fig. 3 is 0.5042, which closely matches the numerically obtained value of 0.4987 in Table 1.) This indicates that the UF is performing in a more optimal manner than the EKF. However, the UF algorithm comes with a computational cost, mainly due to the covariance decomposition. Our experience has shown that the UF algorithm is about two times slower than the EKF algorithm. Still, the performance enhancements

Table 2 Results using simulated magnetic field data with colored noise

Parameter	Truth	TWOSTEP	Centered	EKF	UF
b_1	50 mG	49.9932 ± 2.0823	49.9924 ± 2.2267	49.1063 ± 3.2992	49.9184 ± 2.2511
b_2	30 mG	29.9046 ± 2.7712	29.8880 ± 33.5958	31.8155 ± 6.8599	29.7986 ± 3.0082
b_3	60 mG	59.9756 ± 2.1223	59.9748 ± 2.8451	57.4531 ± 3.7594	59.9080 ± 2.2783
D_{11}	0.05	0.0502 ± 0.0010	0.0502 ± 0.0015	0.0489 ± 0.0015	0.0499 ± 0.0014
D_{22}	0.10	0.0997 ± 0.0105	0.1002 ± 0.0747	0.1127 ± 0.0301	0.0994 ± 0.0116
D_{33}	0.05	0.0501 ± 0.0010	0.0503 ± 0.0026	0.0491 ± 0.0015	0.0499 ± 0.0014
D_{12}	0.05	0.0500 ± 0.0047	0.0499 ± 0.0051	0.0481 ± 0.0080	0.0498 ± 0.0052
D_{13}	0.05	0.0498 ± 0.0009	0.0498 ± 0.0016	0.0499 ± 0.0007	0.0500 ± 0.0006
D_{23}	0.05	0.0499 ± 0.0047	0.0498 ± 0.0059	0.0445 ± 0.0082	0.0498 ± 0.0052

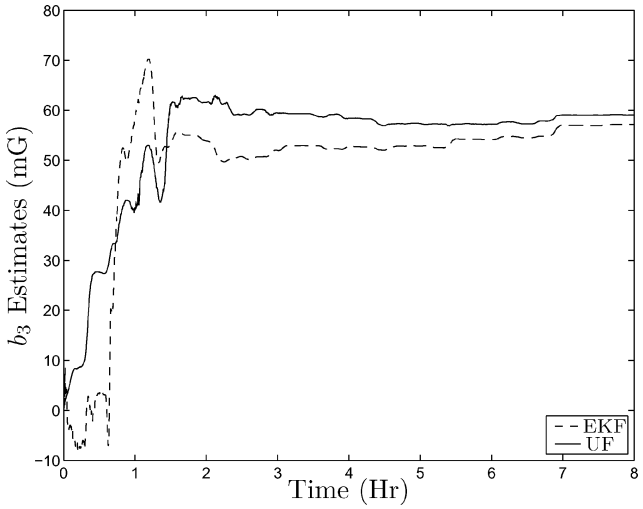

Fig. 4 EKF and UF estimates for b_3 with colored noise.

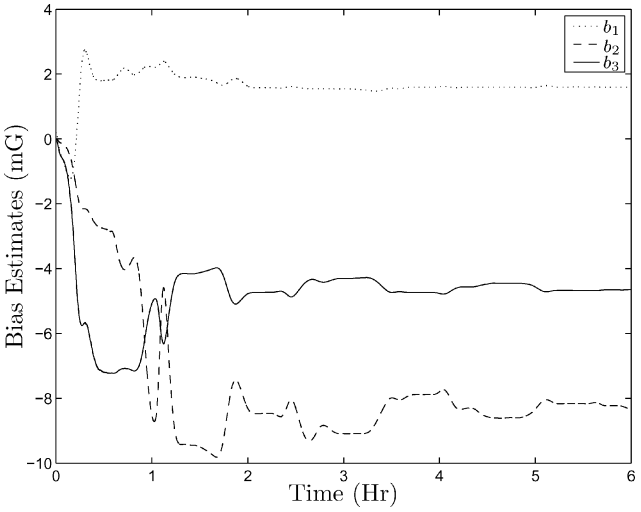

Fig. 5 EKF bias estimates using real TRACE data.

of the UF over the EKF may outweigh the increased computational costs.

The robustness of the real-time algorithms is now tested by adding colored noise to the measurements, which more closely models the actual geomagnetic field errors. This noise is modeled using the colored noise model shown in Ref. 9. The initial conditions and covariances are the same as the earlier simulation. Shown in Table 2 are the averaged batch solutions given by the TWOSTEP, sequential centered, EKF, and UF algorithms, each with their 3σ bounds obtained. Larger deviations are present for all of the algorithms due to the colored-noise process. Also note that the actual errors are outside the bounds computed from the covariance of all of the estimators based on the now incorrect assumptions of the measurement noise.[9] As in the white-noise case, the sequential centered algorithm has a wide of variation in the b_2 parameter. A surprising outcome is given for the EKF algorithm because it is now performing better with the colored-noise model, in contrast to the results of the preceding simulation using white-noise errors only. This may be due to an increased observability from the artificial "motion" induced by the colored noise. Figure 4 shows the convergence of b_3 for both the EKF and UF. Even though the EKF estimates converge to nearly the same value as the UF estimates, the UF converges near the true value of 60 mG much faster than the EKF. Similar results are seen in the other parameters as well. Both simulation results, one using white-noise errors only and the other using colored-noise errors, indicate that the UF provides the most robust real-time algorithm in terms of both overall accuracy and convergence properties.

Next, results using real data from the TRACE spacecraft are shown. This is an sun-synchronous spacecraft in low Earth orbit (currently at about 600 km). The data collected for the spacecraft are given during an inertial pointing mode. The errors associated with the geomagnetic field model are typically spacially correlated and may be non-Gaussian in nature (see Ref. 19). This violates the assumptions for all of the estimators shown in this paper. We still assume that the measurement noise is white and Gaussian, but the standard deviation is now increased to a value of 3 mG, which bounds the errors in a practical sense. The measurements are sampled every 3 s over a 6-h span.

The EKF and UF are both executed at time $t = 0$ using initial conditions of zeros for all states. The initial covariance matrix is diagonal, given by

$$P_0 = \begin{bmatrix} 10 I_{3\times 3} & 0_{3\times 3} \\ 0_{6\times 3} & 0.001 I_{6\times 6} \end{bmatrix} \tag{23}$$

This assumes a 3σ bound on the initial bias estimates to be about 10 mG, and a 3σ bound on the initial estimates for the elements of the D matrix to be about 0.1. The parameters used in the UF are $\alpha = 0.1$, $\beta = 300$, $\kappa = 3 - n$, and $n = 9$. For the real data, the solutions obtained using TWOSTEP and the EKF and UF algorithms at the final time are nearly identical. This is most likely due to the well-behaved nature of the data, that is, the calibration errors are small. Also, the convergence rate and 3σ bounds of the EKF and UF are nearly identical. However, the sequential centered algorithm gave slightly different results. The centered algorithm final results are given by

$$\boldsymbol{b}^* = [1.4007 \quad -8.7350 \quad -3.7927]^T \tag{24a}$$

$$D^* = [0.0086 \quad 0.0437 \quad 0.0065 \quad 0.0006 \quad 0.0035 \quad -0.0120]^T \tag{24b}$$

The TWOSTEP, EKF, and UF final results are given by

$$\boldsymbol{b}^* = [1.6056 \quad -8.4140 \quad -4.6123]^T \tag{25a}$$

$$D^* = [0.0123 \quad 0.0181 \quad 0.0040 \quad -0.0005 \quad 0.0038 \quad -0.0019]^T \tag{25b}$$

Figure 5 shows EKF estimates for the bias vector $\boldsymbol{b}$. Figure 6 shows the 3σ bounds for the bias estimates. Note that the bias estimates

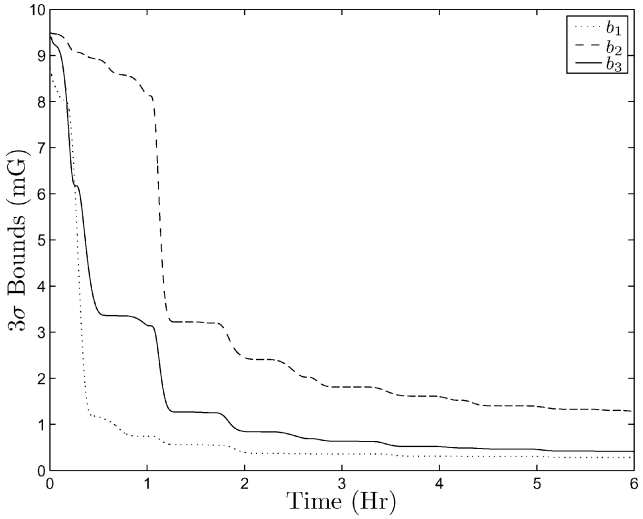

Fig. 6 EKF 3σ bounds using real TRACE data.

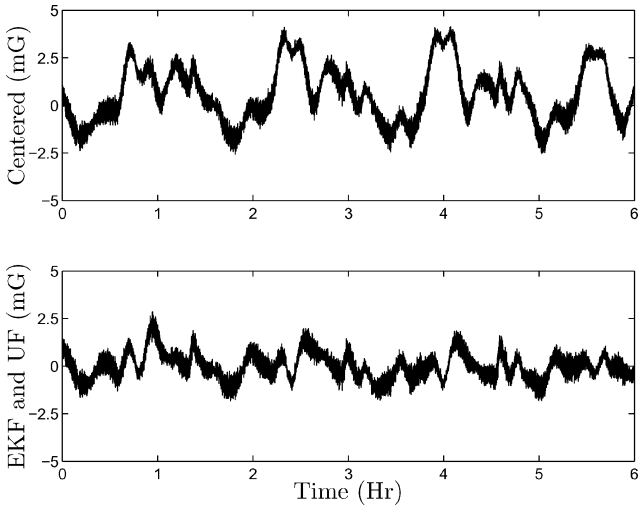

Fig. 7 Norm residual using real TRACE data.

with the larger 3σ bounds have greater variability, which is due to the relative observability between parameters; b_2 is the least observable parameter in this case. Similar results are obtained for the D matrix parameters.

An investigation of the residuals between the norm of the estimated vector, using the calibrated parameters and the geomagnetic-reference vector is useful to check the consistency of the results. These residuals are shown in Fig. 7. A spectrum analysis shows the presence of sinusoidal motions with periods equivalent to the orbital period ($\approx$90 min) and higher-order harmonics. (See Ref. 19 for a model of this process.) The mean value for the sequential centered residuals is 0.60 mG, whereas the mean value for the EKF and UF residuals is only 0.02 mG. Also, the magnitudes of the EKF and UF residuals are smaller than the centered residuals.

Conclusions

Three real-time algorithms were developed for the calibration of TAMs. The sequential centered algorithm was derived from a linear least-squares approach based on a centering approximation. The other algorithms were derived using the EKF and UF. Simulated Monte Carlo test cases showed that the UF gave accurate results with the least amount of variation compared to the other real-time algorithms and is very robust to realistic nonwhite noise errors. Results using real data indicated that the residuals from the EKF and UF algorithms have mean closer to zero and have smaller magnitudes than the residuals from the sequential centered algorithm. Taken together, the simulation and real data results indicate that the UF provided the most robust real-time algorithm in terms of both overall accuracy and convergence properties. Therefore, this algorithm is recommended for actual implementation when computational requirements are not burdensome.

Acknowledgments

The first two authors were supported by NASA Goddard Space Flight Center Grant NAG5-12179. These authors greatly appreciate this support. Also, the authors thank Malcolm D. Shuster for many helpful discussions and insights.

References

[1]Blaylock, B. T., "Magnetometers," *Spacecraft Attitude Determination and Control*, edited by J. R. Wertz, Kluwer Academic, Dordrecht, The Netherlands, 1978, Chap. 6.3, pp. 180–184.

[2]Psiaki, M. L., Martel, F., and Pal, P. K., "Three-Axis Attitude Determination via Kalman Filtering of Magnetometer Data," *Journal of Guidance, Control, and Dynamics*, Vol. 13, No. 3, 1990, pp. 506–514.

[3]Challa, M., and Natanson, G., "Effects of Magnetometer Calibration and Maneuvers on Accuracies of Magnetometer-Only Attitude and Rate Determination," *Proceedings of the AAS/GSFC 13th International Symposium on Space Flight Dynamics*, Vol. 1, NASA CP-1998-206858/VOL1, NASA Goddard Space Flight Center, Greenbelt, MD, 1998, pp. 389–401.

[4]Deutschmann, J. K., and Bar-Itzhack, I., "Evaluation of Attitude and Orbit Estimation Using Actual Earth Magnetic Field Data," *Journal of Guidance, Control, and Dynamics*, Vol. 24, No. 3, 2001, pp. 616–623.

[5]Jung, J., and Psiaki, M. L., "Tests of Magnetometer/Sun-Sensor Orbit Determination Using Flight Data," *Journal of Guidance, Control, and Dynamics*, Vol. 25, No. 3, 2002, pp. 582–590.

[6]Alonso, R., and Shuster, M. D., "Complete Linear Attitude-Independent Magnetometer Calibration," *Journal of the Astronautical Sciences*, Vol. 50, No. 4, 2002, pp. 477–490.

[7]Lerner, G. M., "Scalar Checking," *Spacecraft Attitude Determination and Control*, edited by J. R. Wertz, Kluwer Academic, Dordrecht, The Netherlands, 1978, Chap. 9.3, pp. 328–334.

[8]Gambhir, B., "Determination of Magnetometer Biases Using Module RESIDG," Computer Sciences Corp., Technical Rept. 3000-32700-01TN, Lanham–Seabrook, MD, March 1975.

[9]Alonso, R., and Shuster, M. D., "TWOSTEP: A Fast Robust Algorithm for Attitude-Independent Magnetometer-Bias Determination," *Journal of the Astronautical Sciences*, Vol. 50, No. 4, 2002, pp. 433–451.

[10]Alonso, R., and Shuster, M. D., "Attitude-Independent Magnetometer-Bias Determination: A Survey," *Journal of the Astronautical Sciences*, Vol. 50, No. 4, 2002, pp. 453–475.

[11]Crassidis, J. L., Markley, F. L., and Lightsey, E. G., "Global Positioning System Integer Ambiguity Resolution Without Attitude Knowledge," *Journal of Guidance, Control, and Dynamics*, Vol. 22, No. 2, 1999, pp. 212–218.

[12]Crassidis, J. L., and Junkins, J. L., *Optimal Estimation of Dynamic Systems*, CRC Press, Boca Raton, FL, 2004, Chap. 5.

[13]Julier, S. J., Uhlmann, J. K., and Durrant-Whyte, H. F., "A New Method for the Nonlinear Transformation of Means and Covariances in Filters and Estimators," *IEEE Transactions on Automatic Control*, Vol. AC-45, No. 3, 2000, pp. 477–482.

[14]Wan, E., and van der Merwe, R., "The Unscented Kalman Filter," *Kalman Filtering and Neural Networks*, edited by S. Haykin, Wiley, New York, 2001, Chap. 7.

[15]Golub, G. H., and Van Loan, C. F., *Matrix Computations*, 2nd ed., Johns Hopkins Univ. Press, Baltimore, MD, 1989, Chap. 4.

[16]Crassidis, J. L., Lai, K.-L., and Harman, R. R., "Real-Time Attitude-Independent Three-Axis Magnetometer Calibration," *Flight Mechanics Symposium*, NASA CP-2003-212246, NASA Goddard Space Flight Center, Greenbelt, MD, Session 6, Paper 5, 2003.

[17]Andrews, S. F., and Bilanow, S., "Recent Flight Results of the TRMM Kalman Filter," AIAA Paper 2002-5047, Aug. 2002.

[18]Langel, R. A., "The Main Field," *Geomagnetism*, edited by J. A. Jacobs, Academic Press, Orlando, FL, 1987, pp. 249–512.

[19]Crassidis, J. L., Andrews, S. F., Markley, F. L., and Ha, K., "Contingency Designs for Attitude Determination of TRMM," *Proceedings of the Flight Mechanics/Estimation Theory Symposium*, NASA CP-3299, NASA Goddard Space Flight Center, Greenbelt, MD, 1995, pp. 419–433.